Int. J. Heat Mass Transfer. Vol. 34, No. 2, pp. 449–459, 1991
Printed in Great Britain

0017–9310/91 $3.00 + 0.00

Double diffusive natural convection in a vertical rectangular enclosure—I. Experimental study

HWATAIK HAN and THOMAS H. KUEHN
Department of Mechanical Engineering, University of Minnesota, Minneapolis, MN 55455, U.S.A.

(*Received* 28 *December* 1989 *and in final form* 6 *April* 1990)

Abstract—Double diffusive natural convection flows in a two-dimensional rectangular enclosure are investigated using an electrochemical technique with the vertical electrodes maintained at different temperatures. Schlieren flow visualization photographs show interesting timewise evolution of multicell flow structures in an enclosure for both aiding and opposing thermal and solutal buoyant forces. Details of the multicell flow characteristics including the temperature and concentration profiles as well as the overall heat and mass transfer characteristics in the cavity are presented.

1. INTRODUCTION

WHEN PARALLEL temperature and concentration gradients are imposed on a natural convective fluid cavity, the two buoyant forces can either enhance or suppress heat and mass transfer rates depending on their direction. In addition to the direction and magnitude of the buoyant forces, the ratio of thermal and solutal diffusivities increases the complexity of the problem. Dimensionless system governing parameters are found to be thermal Grashof number, solutal Grashof number, Prandtl number, and Schmidt number for a given geometry with a given set of simple boundary conditions.

Studies on double diffusive convection were initiated by oceanographers. Much of the theoretical work has developed from linear stability theory for a simple salt-stratified fluid heated from below. The definition of double diffusive convection has been confined to cases in which (1) the diffusivities differ considerably and (2) two buoyant forces oppose each other [1]. The considerable difference in diffusivities between heat and salt have exhibited many interesting double diffusive convection phenomena, such as salt fingers and sharp diffusive interfaces. More recently, transitional layered flow structures have been observed by lateral heating in a stably salt stratified fluid [2].

Only a few studies on double diffusive natural convection in an enclosed cavity are available in the literature in which both temperature and concentration gradients are imposed laterally. Hu and El-Wakil [3] conducted simultaneous heat and mass transfer experiments in an enclosure using air–water and air–n-heptane systems. Flow fields observed were similar to pure thermal convection in a cavity, since the Lewis number was not considerably different from unity. Electrochemical experiments performed by Kamotani *et al.* [4] for application to crystal growth processes reported layered flow structures in shallow enclosures. More recently, Lee *et al.* [5] conducted an experiment using the osmosis process from vertical membrane walls and presented photographs showing steady multicell flow structures.

However, none of the previous investigations have exhibited how a multicell flow structure develops from a unicell motion in a vertical rectangular cavity. In the present paper, the double diffusive natural convection experiment is extended to a wider range of system parameters in different aspect ratio cavities, and transient flow visualization photographs showing the detailed information on the formation of the double diffusive multicell flow structure are presented. Other measured quantities, such as temperature and concentration profiles in the cavity as well as heat and mass transfer rates provide additional information in understanding the double diffusive multicell flow structures. Two aspect ratios are considered, $H/L = 1$ and 4. The thermal Grashof number range is 1.4×10^5–1.1×10^6, and the solutal Grashof number range is 2.7×10^6–1.8×10^7. The Prandtl number and Schmidt number of the fluid range between 7.8–8.8 and 2300–2600, respectively.

2. EXPERIMENTAL APPARATUS

A test setup has been constructed to model a two-dimensional vertical rectangular enclosure which can impose horizontal temperature and concentration gradients in the fluid. A schematic diagram of the test section is shown in Fig. 1. The active parts of the test section are two vertical electrodes; the anode and cathode, which have been constructed of 6.4 mm thick copper plate with dimensions of 50.8×152.4 mm (height × length). The anode is the mass source electrode where a positive potential is applied during electrochemical experiments, and the cathode is the mass sink with a uniform concentration of zero under limiting current conditions. Chromel wires of 30 gage, used as heating elements, are glued in seven equally spaced

NOMENCLATURE

C	molar concentration of cupric ions [mol l^{-1}]
c	dimensionless concentration, $(C-C_{low})/(C_{high}-C_{low})$
ΔC	concentration difference between the electrodes, $(C_{high}-C_{low})$
D	diffusion coefficient of cupric ions in aqueous solution [$m^2 s^{-1}$]
g	gravitational acceleration [$m s^{-2}$]
Gr_M	solutal Grashof number, $g\beta_m\Delta CH^3/\nu^2$
$Gr_{M\,eff}$	effective solutal Grashof number
Gr_T	thermal Grashof number, $g\beta_t\Delta TH^3/\nu^2$
$Gr_{T\,eff}$	effective thermal Grashof number
H	height of the enclosure [m]
h	heat transfer coefficient [$W m^{-2} °C^{-1}$]
h_m	mass transfer coefficient [$m s^{-1}$]
k	thermal conductivity [$W m^{-1} °C^{-1}$]
L	width of the enclosure [m]
Le	Lewis number, Sc/Pr
N	buoyancy ratio, $\beta_m\Delta C/\beta_t\Delta T$ or Gr_M/Gr_T
Nu	Nusselt number, hH/k
Pr	Prandtl number, ν/a
Sc	Schmidt number, ν/D
Sh	Sherwood number, h_mH/D
T	temperature [°C]
t	dimensionless temperature, $(T-T_{cold})/(T_{hot}-T_{cold})$
ΔT	temperature difference between the electrodes, $(T_{hot}-T_{cold})$
X	horizontal coordinate [m]
Y	vertical coordinate [m].

Greek symbols

α	thermal diffusivity [$m^2 s^{-1}$]
β_m	solutal volumetric expansion coefficient [$l mol^{-1}$]
β_t	thermal volumetric expansion coefficient [$°C^{-1}$]
ν	kinematic viscosity [$m^2 s^{-1}$].

horizontal grooves (1.0 × 1.0 mm) machined into the back surfaces of the copper electrodes. Five T-type (copper–constantan) thermocouple wires (30 gage) are installed in each copper plate to measure the temperature of the electrodes. The heat loss through the perimeter is reduced by machining a step in the edges of the plates. To measure local mass transfer rates, seven circular electrodes (1.00 mm in diameter) are installed evenly spaced along the vertical centerline of the cathode. Each probe is electrically insulated from the host copper plate by a 0.038 mm annular gap filled with epoxy. The copper plates are placed in plexiglas housings, which have water jackets for cooling water to circulate through. The distance between the assembled electrodes is maintained with top and bottom polystyrene spacers, on which thin sheets of plexiglas (1.6 mm) are glued to provide smooth surfaces. The assembled test section is contained in a 154 × 154 × 154 mm chamber. The end walls of the chamber are made of optical glass to accommodate the flow visualization study.

The test enclosure is filled with electrolyte solution,

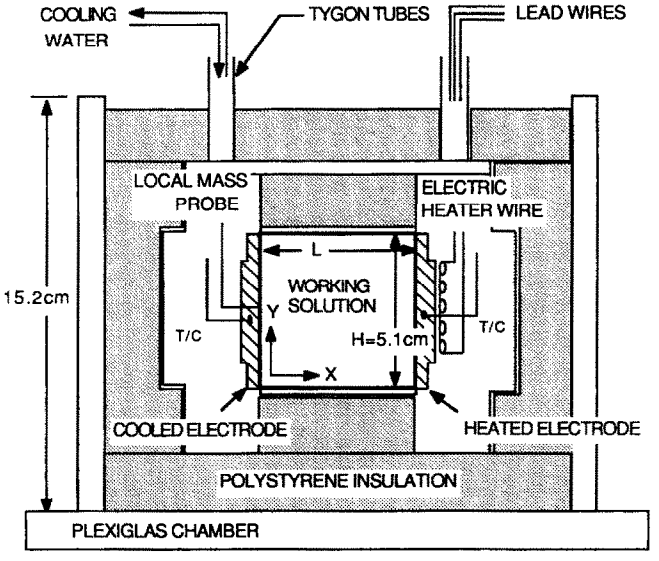

FIG. 1. Assembled test chamber.

which is an aqueous solution of cupric sulfate with sulfuric acid as a supporting electrolyte to suppress the effect of migration of cupric ions by electric potential gradients. Natural convection driven by density gradients is considered to be the only convective transport mechanism of heat and mass in the solution. The cupric ions are the transferred ions which dissolve from the anode and plate out on the cathode. Details on electrochemistry can be found in the literature [6]. The property values given by Eisenberg *et al.* are used in the present study [7].

A schematic diagram of the overall experimental setup is presented in Fig. 2. The thermocouple wires are attached to an isothermal junction, and an ice bath is used as the reference temperature. The wires from the electrodes, local mass probes, and heater elements are connected to a central circuit board, where all the electric circuitry is connected. A 0.1 Ω (±0.5%) calibrated precision resistor serves as a current shunt for measurements of overall mass transfer rates. For the local mass probes, 1.0 kΩ resistors (±1%) serve as current shunts. The shunt resistors have been chosen to keep the voltage drop across the shunt resistors small in order to apply the same uniform voltage to the cathode and the local mass probes. Voltages of the power supplies and output signals from thermocouples and shunt resistors are recorded by an HP-3421 automatic data acquisition system connected to an HP-86 computer.

Flow visualization has been accomplished using the Schlieren method. A 5 mW helium–neon gas laser is used as the light source. The emitted beam is expanded into a parallel beam of about 10 cm diameter by an objective lens (20×), and a collimating lens of a focal length of 600 mm. The collimated laser beam is transmitted through the electrolytic cell where it is deflected by the gradient of refractive index in the electrolyte solution. The beam is collected by a concave spherical mirror ($f = 300$ mm), and focused onto a screen. The refracted beam either adds to or subtracts from the light normally present on the screen. The position of the knife edge may be adjusted near the focal plane of the concave mirror to obtain a sharp image by cutting off a part of the refracted light beam effectively. Details of the Schlieren method can be found in the literature [8]. The image on the screen is recorded with a VHS 1.2 in. video camcorder.

3. EXPERIMENTAL PROCEDURE

After each experiment, the enclosure is disassembled and the surfaces of the electrodes are polished, starting with an emery paper #200, down to #600 sequentially. Care was taken in polishing around the local mass probes on the cathode in order not to bridge over the insulation gap. The plates are washed freely with tap water, then distilled water. Technical grade methanol is applied finally to dry the surface and to increase the wetting action of the electrolyte solution.

In order to eliminate the tedious conventional polishing procedure, an electropotential reversal technique had been attempted to remove the copper deposited on the cathode surface. The cathode surface had been electroplated with stable metals, i.e. silver and gold. The silver plating was so thick that it bridged

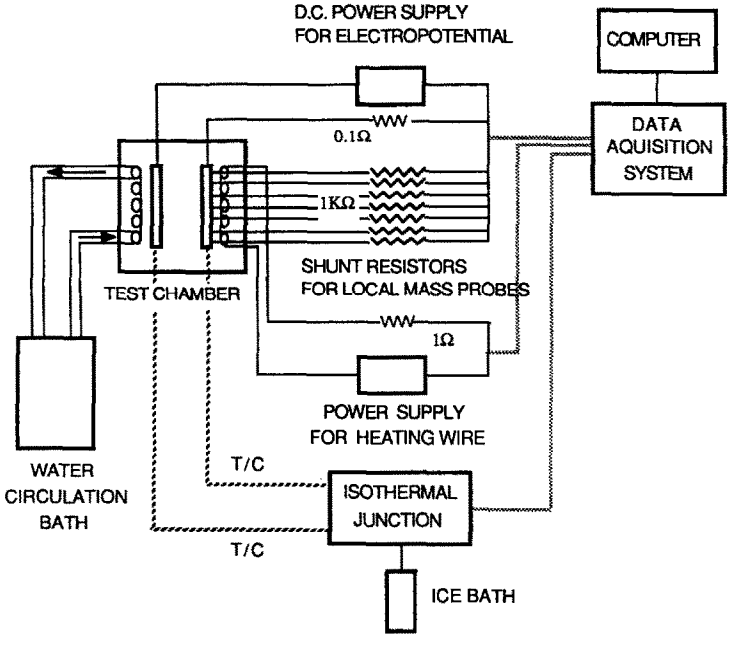

FIG. 2. Schematic of overall experimental setup.

over the insulation gaps of the local mass probes, and it oxidized during voltage reversals. Thin gold plating partially peeled off after several voltage reversals due to imperfect bonding. This plating technique was not pursued further. The conventional polishing procedure described above was used for this study.

The assembled enclosure cell is placed into the test chamber, and the electrolyte solution is added to the cell. Gas bubbles are allowed to escape from the test enclosure. The range of typical bulk concentration of cupric ions is between 0.015–0.05 mol l^{-1}, and the sulfuric acid concentration is 1.5 mol l^{-1}. The entire test chamber is insulated with 5.1 mm thick polystyrene sheet on the exterior.

An experiment begins after initial disturbances disappear in the solution. Heat transfer conditions are established prior to initiating mass transfer. One electrode is connected to a d.c. power supply and the other electrode is connected to a water circulation bath. The circulation bath has a large water flow rate so that the change in temperature across the water jacket is less than 0.02°C at maximum power input. The bulk temperature of the solution is maintained at room temperature to minimize heat transfer with the ambient. The range of ΔT between electrodes is 0.5–10°C. More than 12 h is required to reach a thermal steady-state condition. The maximum temperature nonhomogeneity of an electrode plate is approximately 0.05°C. Errors due to nonuniformity of the isothermal junction, and errors of thermocouple calibration are considered to be negligible.

After a thermal steady-state condition is reached, electropotential for the mass transfer system is switched on. Mass transfer data as well as heat transfer data are monitored every 30 s. All the experiments are performed under limiting current conditions, which corresponds to zero concentration of transferred ion at the cathode surface. Concentration of the cupric ions on the anode surface is not constant in reality. However, the average change in concentration across the boundary layer on the anode is equal to the concentration difference between the bulk fluid and the cathode surface, which is zero. Concentration of the cupric ions on the anode surface is considered to be twice the bulk concentration by assuming symmetry of the flow near the cathode and anode [4]. A current density vs electropotential voltage curve shows a limiting current plateau between 0.55 and 0.59 V for the present conditions. The properties of the solution are assumed to be constant and are determined at the bulk temperature and the bulk concentration of the solution.

When steady conditions are reached, temperature and concentration profiles are measured in the solution. To measure the temperature distributions, a thermocouple probe is utilized, which has been designed and fabricated to minimize the disturbances in the flow field and to eliminate the axial conduction error along the thermocouple wires. A chromel–constantan thermocouple butt joint of 36 gage wire is covered with a thin film of Glyptal paint to protect it from the acid solution. The thermocouple wires are stretched between the end walls of the test enclosure and are connected to a two-pronged fork. The probe is translated with a two-way traveling vice equipped with linear rheostats for position measurement. Approximately 1 min is allowed for the thermocouple junction to reach thermal equilibrium at each new position.

The concentration distribution of cupric ions in the solution is determined by measuring the attenuation of light through the test cell. According to Beer's law, the concentration of a solution is proportional to an absorbance, which is defined as the logarithm of the ratio of input and output light intensities. A He–Ne laser (5 mW) is used as the light source. The laser beam (2 mm diameter) is aligned with a photo diode, and the test cell is placed between. The entire test cell is moved vertically on a calibrated laboratory jack. Absorbance through the test cell has been calibrated with well-mixed electrolyte solutions of known cupric ion concentration. The error range of the concentration measurements is of the order of 5%. A more detailed description of the apparatus is available in ref. [9].

4. RESULTS AND DISCUSSION

4.1. *Aspect ratio* = 4

4.1.1. *Aiding buoyancy case.* The transient behavior of the flow motion for an aiding buoyancy case is shown in Fig. 3. Figure 3(a) shows steady-state pure thermal convection at $Gr_T = 3.8 \times 10^5$. The left vertical wall is a cold anode, and the right wall is a hot cathode. Fluid rotates in a counter-clockwise direction in a single cell.

When the mass potential is applied at time zero, thin concentration boundary layers develop inside the existing relatively thick thermal boundary layers on the vertical plates. On the cathode surface (the right wall), a plume of low concentration fluid, which has a high temperature, reaches the top of the enclosure and progresses to the other side of the enclosure (Fig. 3(b)). The number under each photograph indicates the time elapsed after the electropotential is applied in hours and minutes. The counter-clockwise core flow driven by the thermal force helps the plume move forward by viscous drag. While traveling along the top wall, the fluid loses its thermal identity, as heat is being transferred to the neighboring core fluid. However, it does not lose the concentration identity, because of the slow solutal diffusion process.

When the fluid approaches the thermal boundary layer on the cold anode surface, the fluid has cooled but retains its low concentration. The fluid cannot be pulled down by the weak downward thermal buoyant force, and remains near the top of the cavity. Note the buoyancy ratio, N, is 8.5 for this experiment. A similar explanation can be applied to the boundary

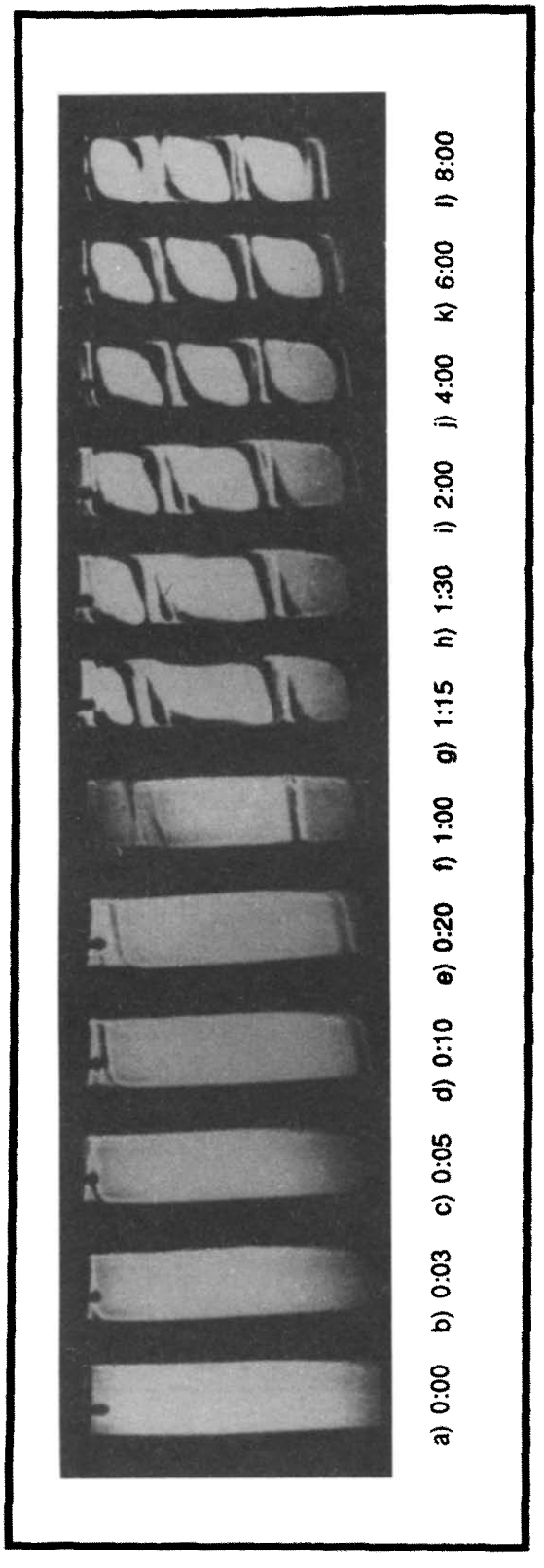

FIG. 3. Schlieren photographs with a horizontal knife edge for transient aiding flow in hours : minutes after start of mass transfer; $H/L = 4$, $Gr_T = 3.8 \times 10^5$, $Gr_M = 3.2 \times 10^6$ ($N = 8.5$).

layers on the anode side and the plume along the bottom wall.

As fluid is pumped into the top and bottom layers from the concentration boundary layers, the thickness of each layer increases. The interfaces with the center cell are shown clearly in Figs. 3(d) and (e). As both layers grow in size, the initial unicell in the center shrinks. Both layers are essentially stagnant until they reach a certain size (Fig. 3(f)). As the layers become thicker, the thermal buoyant forces due to the temperature difference of the vertical side walls overcomes the shear forces at the interfaces between the layers and the center cell. The fluid in the layers begins to rotate in the same direction as the center cell (counterclockwise), and a distinct three cell structure is formed in the enclosure.

Each cell behaves as a separate cell. Fluid flows in opposite directions on each side of the interfaces between cells, and creates a high shear. Across the interfaces steep temperature and concentration gradients exist as well as large velocity gradients. Each cell has nearly uniform concentration due to efficient thermal mixing. In Figs. 3(g)–(i), the top and bottom cells grow and become nearly equal in size with the center cell. Figure 3(j) can be considered a steady-state condition because the flow structure does not change significantly afterwards (Figs. 3(k) and (l)). The time duration of the experiments is limited by the roughening of the cathode surface. As cupric ions deposit on the cathode surface, the surface becomes rough, and the mass transfer rate increases slowly after 5–6 h for the present experiments. The rate of surface roughening depends on the local mass transfer rate and is therefore nonuniform on the cathode. Figure 4 shows time-wise variations of mass transfer rates from local mass probes on the cathode surface. After 1 h some of the probes show rapid increases in mass transfer due to copper deposition on the insulation gaps. The data between 0.5 and 1 h show the monotonic decrease of mass transfer rate with distance along the surface that is expected.

4.1.2. *Opposing buoyancy case.* In Fig. 5, the cold cathode appears on the left, and the hot anode on the right. Figure 5(a) shows the thermal steady state in which the fluid is rotating counter-clockwise. When the mass potential is superimposed on the system, thin concentration boundary layers develop on the electrode surfaces. The fluid inside the concentration boundary layers has opposing solutal and thermal buoyant forces. Since the solutal Grashof number is greater than the thermal Grashof number for the present experiment ($N = 6.5$), the solutal buoyant force overcomes the thermal buoyant force, which initiates flow in the direction opposite to the pre-existing thermal motion. There is a high shear region between the thermal boundary layer and the concentration boundary layer.

On the cathode surface, a plume of fluid of low concentration in the concentration boundary layer reaches the top wall and progresses to the anode, as in the aiding case. The plume motion is, however, much slower than in the aiding case, since the front of the plume is creeping against the overall unicell motion driven by the thermal buoyant force (Fig. 5(b)). As the cold plume travels along the top wall, it gains heat from the neighboring fluid moving in the other direction. The mechanism is similar to a counterflow heat exchanger, whereas the aiding case is like a parallel flow heat exchanger. Near the top of the hot anode, the cold plume meets a hot thermal plume from the anode surface. The interface becomes complex and causes the thermal plume to separate from the hot anode surface (Fig. 5(e)). A similar phenomena occurs with the plume along the bottom wall.

The top and bottom layers are initially stagnant. As they grow in size, thermal convection becomes important in the layers (Fig. 5(f)). In Figs. 5(f)–(i), the cells continue growing, while rotating in the same

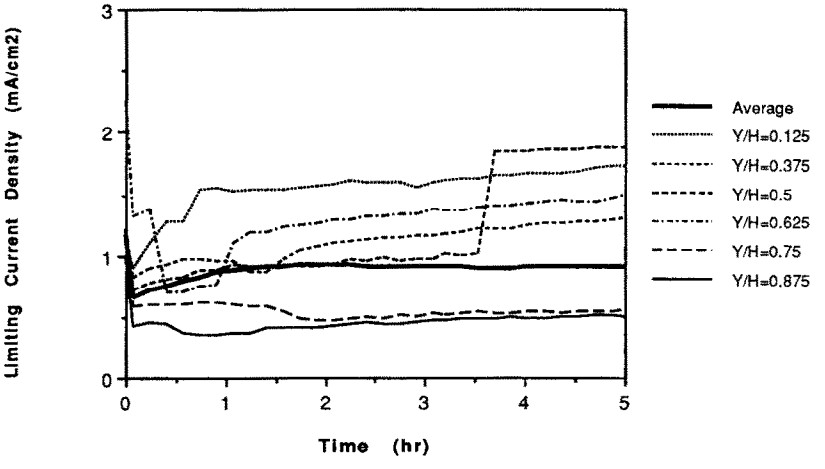

FIG. 4. Local mass transfer rates measured by local mass probes on cathode surface, $H/L = 4$, $Gr_T = 3.8 \times 10^5$, $Gr_M = 3.2 \times 10^6$.

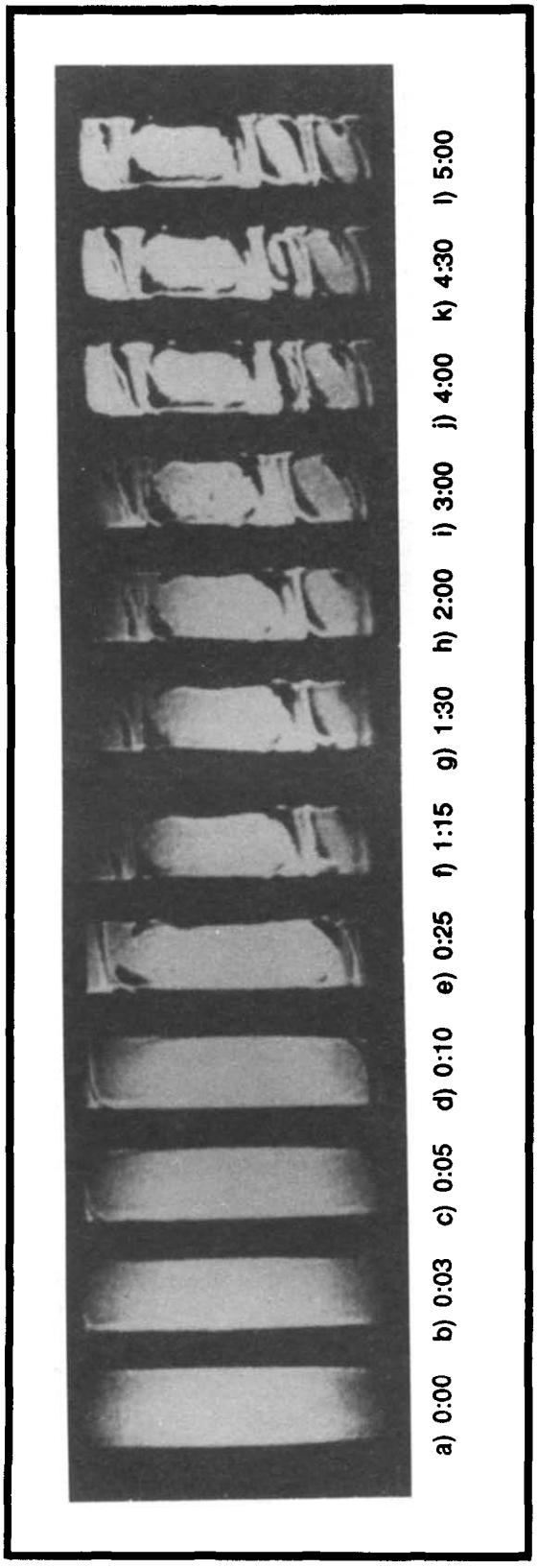

FIG. 5. Schlieren photographs with a horizontal knife edge for transient opposing flow in hours : minutes after start of mass transfer; $H/L = 4$, $Gr_T = -5.0 \times 10^5$, $Gr_M = 3.2 \times 10^6$ ($N = -6.5$).

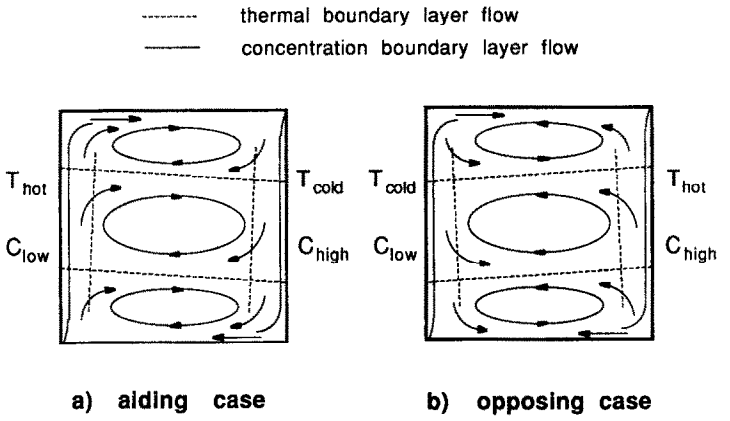

FIG. 6. Multicell flow pattern sketches for $N = 6$–12, $Le = 240$–290 in an enclosure of $H/L = 1$.

counter-clockwise direction as the center cell. However, the growth rate of the cells is slower than in the aiding flow case. The solution has stratified into three cells as in the aiding flow case. In each cell, the thermal and solutal buoyant forces interact in a very complicated fashion. At a later time, a new cell forms between the bottom cell and the center cell (Fig. 5(j)). In Figs. 5(k) and (l), the new cell has grown in size considerably, and the center cell has moved up. The cells do not change significantly afterwards.

4.2. *Aspect ratio* = 1

Similar flow structures are observed for an aspect ratio of $H/L = 1$ for similar values of the buoyancy ratio. Photographs are not included here but flow pattern sketches are shown in Fig. 6. In both aiding and opposing cases, a thin concentration boundary layer covers the entire cathode surface, and passes across the interfaces between cells. However, the thermal plume in the relatively thick thermal boundary layer cannot penetrate into a neighboring cell for the present range of parameters. It only pushes up the interface, and causes the interface to be slightly inclined.

The top cell is observed to be slightly larger than the bottom cell in both aiding and opposing flow cases. Dependence of solution thermo-physical properties on temperature and concentration may contribute to the unsymmetrical behavior. This behavior may also be due to the nature of the vertical boundary conditions. The assumption of an iso-concentration boundary condition may not be valid on the anode surface.

4.3. *Temperature and concentration profiles*

Figure 7 shows temperature and concentration profiles measured in the vertical midplane of the enclosure of aspect ratio, $H/L = 1$, under steady flow conditions. The results are normalized with ΔC and ΔT, differences of concentration and temperature between the cathode and anode surfaces, respectively.

For the pure heat transfer case, the temperature profile shows a continuous increase in temperature with height as expected (Fig. 7(a)). The concentration profile in the fluid is uniform, as heat transfer does not create concentration gradients. The variation of concentration in the enclosure is within experimental error ($\pm 3\%$). For pure mass transfer in isothermal conditions, the concentration measurements show a smooth monotonically decreasing concentration profile (Fig. 7(b)), and the temperature is uniform in the cavity to within experimental uncertainty.

For the aiding flow case, measurements are made 5 h after the mass potential is started, at $Gr_T = 5.2 \times 10^5$, $Gr_M = 3.6 \times 10^6$. Temperatures are stably stratified in each cell, and at the interface between the top two cells, the temperature stratification is inverted. However, between the bottom two cells, the temperature is observed to be nearly uniform. The size of the bottom cell is smaller than the top cell, and convection is not as dominant as in the top cell. The variation in fluid viscosity may partly explain the unsymmetrical behavior, since the fluid viscosity is larger for a fluid of high concentration and low temperature in the bottom cell.

For the opposing flow case, measurements are made 6 h after the mass potential is initiated at $Gr_T = 3.3 \times 10^5$, $Gr_M = 3.2 \times 10^6$. In this case, the fluid supplied to the top cell through the concentration boundary layer is cold and the fluid supplied to the bottom cell is warm. This creates temperature inversions in the top and bottom cells. Temperature stratification in the center of the enclosure in both aiding and opposing cases is larger than that of the pure heat transfer case.

The concentration profile verifies the existence of the distinct cells. It is interesting to note that concentrations are uniform in the top two cells, regardless of aiding or opposing buoyancy. Sharp concentration gradients exist across the interfaces. The color differences between the cells due to the difference in cupric

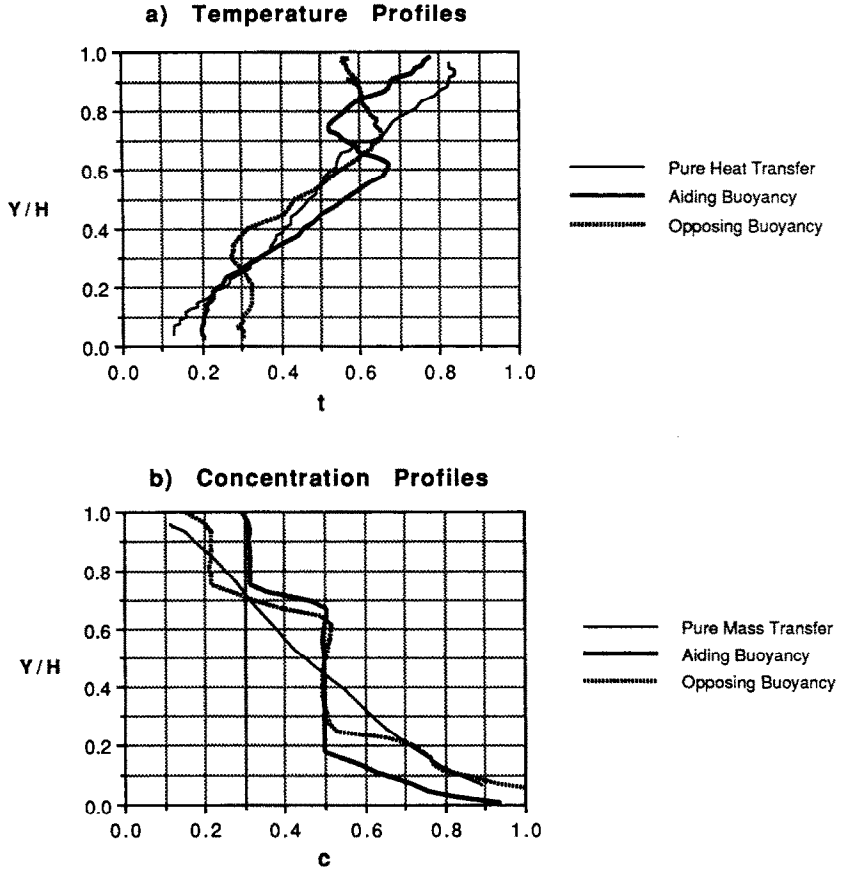

FIG. 7. Steady-state temperature and concentration profiles in an enclosure of $H/L = 1$: pure heat transfer, $Gr_T = 3.6 \times 10^5$; pure mass transfer, $Gr_M = 6.2 \times 10^6$; aiding buoyancy, $Gr_T = 4.8 \times 10^5$, $Gr_M = 3.2 \times 10^6$; opposing buoyancy, $Gr_T = -3.7 \times 10^5$, $Gr_M = 3.2 \times 10^6$.

ion concentration can be readily noticed with the naked eye.

Temperature profiles measured along the horizontal centerline for the aiding and opposing buoyancy conditions present distributions similar to that of thermal natural convection. Concentration profiles show uniform distributions along the horizontal centerline except near the vertical walls. The thin concentration boundary layer could not be resolved with the present experimental setup.

4.4. *Overall heat and mass transfer rates*

The overall heat and mass transfer rates are given in Table 1 and are plotted in Fig. 8 to attempt to correlate the Nusselt and Sherwood numbers as a function of a single variable. The experimental error in the values of Nu and Sh is estimated to be $\pm 10\%$. The Nusselt number is expressed as a function of effective thermal Grashof number times the Prandtl number, and the Sherwood number is expressed as a function of effective solutal Grashof number times the Schmidt number. The effective Grashof numbers are defined as the summations of the two Grashof numbers with a weighting of the square root of the Lewis number [10]

$$Gr_{T\,\mathrm{eff}} = Gr_T + \sqrt{\left(\frac{1}{Le}\right)} Gr_M \tag{1}$$

$$Gr_{M\,\mathrm{eff}} = Gr_M + \sqrt{(Le)}\, Gr_T. \tag{2}$$

The superimposed curve represents the pure heat transfer correlation curve proposed in ref. [11], which combines the correlations in the conduction regime, laminar boundary layer regime, and turbulent regime

$$Nu = [Nu_{\mathrm{conv}}^{15} + Nu_{\mathrm{cond}}^{15}]^{1/15} \tag{3}$$

where $Nu_{\mathrm{cond}} = H/L$, and

$$Nu_{\mathrm{conv}} = \frac{1}{2}\left[\left(0.67Ra^{0.25}\left[1+\left(\frac{0.559}{Pr}\right)^{0.6}\right]^{(-5/12)}\right)^{15} + (0.1Ra^{1/3})^{15}\right]^{(1/15)}.$$

The pure heat transfer data fall within $\pm 20\%$, and

Table 1. List of experimental results

Aspect ratio	Gr_T	Gr_M	N	Pr	Sc	$\overline{Nu}$	Sh
$H/L = 1$	2.0×10^5	0	0	8.5	—	10.6	—
	3.6×10^5	0	0	8.4	—	12.2	—
	6.7×10^5	0	0	8.5	—	15.0	—
	0	3.1×10^6	∞	—	2390	—	101
	0	6.1×10^6	∞	—	2420	—	126
	0	6.2×10^6	∞	—	2420	—	127
	-3.7×10^5	3.2×10^6	−8.6	8.5	2390	5.3	92
	-1.1×10^6	6.8×10^6	−6.3	8.4	2420	9.5	83
	4.8×10^5	3.2×10^6	6.7	8.5	2390	9.0	154
	8.0×10^5	6.7×10^6	8.4	8.4	2410	13.0	153
	2.6×10^5	3.2×10^6	12.5	8.5	2390	8.1	123
$H/L = 4$	3.4×10^5	0	0	8.8	—	11.6	—
	3.7×10^5	0	0	8.0	—	13.2	—
	5.6×10^5	0	0	8.5	—	17.1	—
	0	3.2×10^6	∞	—	2390	—	103
	0	5.5×10^6	∞	—	2360	—	120
	0	1.1×10^7	∞	—	2550	—	150
	0	1.8×10^7	∞	—	2440	—	176
	-3.1×10^5	7.0×10^6	−23.1	8.5	2390	2.8	116
	-5.0×10^5	9.0×10^6	−18.0	8.9	2460	6.9	112
	-4.5×10^5	6.5×10^6	−14.4	8.0	2430	7.5	128
	-5.0×10^5	3.2×10^6	−6.5	8.5	2390	8.4	113
	-7.4×10^5	3.2×10^6	−4.3	8.6	2390	12.7	90
	-1.8×10^5	2.7×10^6	−1.5	7.7	2400	20.8	121
	3.8×10^5	3.2×10^6	8.5	8.5	2390	11.5	163
	4.8×10^5	6.2×10^6	12.7	7.8	2410	13.9	185

the pure mass transfer data fall within ±15% from the curve obtained at $Pr = 1$ and $H/L = 1$. The correlation is a weak function of aspect ratio and Prandtl number larger than 1. The data points for aiding buoyancy and opposing buoyancy when one of the buoyant forces is dominant over the other also fall closely to the curve. However, the data points for opposing buoyancy are widely scattered especially when the buoyant forces are of the same order of magnitude. A comprehensive correlation equation has not been obtained since there is a lack of data points on transfer rates, and the existing data points are scattered too widely. The effective Grashof numbers defined above have been mostly used for thermal dominant, or solutal dominant flows or when the Lewis number is near unity.

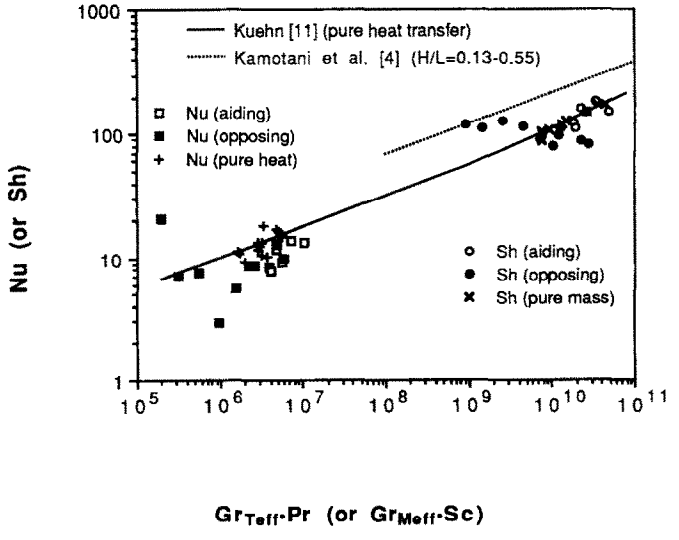

FIG. 8. Overall heat and mass transfer rates shown with a correlation for pure heat transfer in a vertical rectangular enclosure, $H/L = 1$ and 4.

5. SUMMARY AND CONCLUSIONS

Complex transient multicell structure is observed for simultaneous heat and mass transfer in a rectangular enclosure for both aiding and opposing buoyancy conditions. The considerable difference in diffusivities presents interesting double diffusive characteristics. The thin concentration boundary layers do not seem to be affected by the presence of the relatively thick thermal boundary layer regardless of its direction and do not contribute to the creation of fluid motion in the core region. They slowly create concentration stratification in a cavity, however, and eventually change the entire flow structure into a multicell structure. The temperature and concentration profiles measured at steady state are unique to double diffusive natural convection. The overall heat and mass transfer rates are scattered too widely to correlate with a single variable, especially for opposing buoyancy flows when the buoyant forces have the same strength. Further studies are required to cover other ranges of parameters and to correlate the overall heat and mass transfer rates at acceptable levels.

REFERENCES

1. J. S. Turner, *Buoyancy Effects in Fluids*. Cambridge University Press, London (1979).
2. C. F. Chen, D. G. Briggs and R. A. Wirtz, Stability of thermal convection in a salinity gradient due to lateral heating, *Int. J. Heat Mass Transfer* **14**, 57–65 (1971).
3. C. Y. Hu and M. M. El-Wakil, Simultaneous heat and mass transfer in a rectangular cavity, *Proc. 5th Int. Heat Transfer Conf.*, Vol. 5, pp. 24–28 (1974).
4. Y. Kamotani, L. W. Wang, S. Ostrach and H. D. Jiang, Experimental study of natural convection in shallow enclosures with horizontal temperature and concentration gradients, *Int. J. Heat Mass Transfer* **28**, 165–173 (1985).
5. J. Lee, M. T. Hyun and K. W. Kim, Natural convection in confined fluids with combined horizontal temperature and concentration gradients, *Int. J. Heat Mass Transfer* **31**, 1969–1977 (1988).
6. J. R. Lloyd, E. M. Sparrow and E. R. G. Eckert, Local natural convection mass transfer measurements, *J. Electrochem. Soc.* **119**, 702–707 (1972).
7. M. Eisenberg, C. W. Tobias and C. R. Wilke, Selected physical properties of ternary electrolytes employed in ionic mass transfer studies, *J. Electrochem. Soc.* **103**, 413–416 (1956).
8. E. R. G. Eckert and R. J. Goldstein, *Measurements in Heat Transfer*. Hemisphere, Washington, DC (1976).
9. H. Han, Double diffusive natural convection in a vertical rectangular enclosure, Ph.D. Thesis, University of Minnesota (1988).
10. E. V. Somers, Theoretical considerations of combined thermal and mass transfer from a vertical flat plate, *J. Appl. Mech.* **23**, 295–301 (1951).
11. T. H. Kuehn, Natural convection heat transfer from a horizontal circular cylinder to a surrounding cylindrical enclosure, Ph.D. Thesis, University of Minnesota (1976).

CONVECTION NATURELLE DOUBLEMENT DIFFUSIVE DANS UNE CAVITE RECTANGULAIRE VERTICALE—I. ETUDE EXPERIMENTALE

Résumé—Les écoulements de convection naturelle doublement diffusive, dans une cavité rectangulaire bidimensionnelle, sont étudiés en utilisant une technique électrochimique avec des électrodes verticales maintenues à des températures différentes. Des photographies de l'écoulement montrent l'évolution au cours du temps de structures multicellulaires dans une cavité pour des forces de flottement thermique et solutale qui s'aident ou qui s'opposent. On présente des caractéristiques de l'écoulement multicellulaire qui incluent les profils de température et de concentration et les caractéristiques du transfert global de chaleur et de masse.

DOPPELT-DIFFUSIVE NATÜRLICHE KONVEKTION IN EINEM SENKRECHTEN RECHTECKIGEN HOHLRAUM—I. EXPERIMENTELLE UNTERSUCHUNG

Zusammenfassung—Die doppelt-diffusive natürliche Konvektion in einem zweidimensionalen rechteckigen Hohlraum wird unter Verwendung eines elektrochemischen Verfahrens mit senkrechten Elektroden unterschiedlicher Temperatur untersucht. Fotografische Schlieren-Aufnahmen zeigen interessante zeitliche Entwicklungen von multizellularen Strömungsstrukturen im Hohlraum sowohl für gleichgerichtete, wie auch für gegengerichtete temperatur- und konzentrationsbedingte Auftriebskraft. Es werden Einzelheiten der multizellularen Strömung vorgestellt: Temperatur und Konzentrationsprofile, sowie das Verhalten des Gesamtwärmeübergangs und des Gesamtstoffübergangs.

КОНВЕКЦИЯ С ДИФФУЗИЕЙ ТЕПЛА И МАССЫ В ВЕРТИКАЛЬНОЙ ПРЯМОУГОЛЬНОЙ ПОЛОСТИ—I. ЭКСПЕРИМЕНТАЛЬНОЕ ИССЛЕДОВАНИЕ

Аннотация—**Естественноконвективные течения с диффузией тепла и массы в двумерной прямоугольной полости исследуюся с использованием электрохимической техники, с вертикальными электродами, на которых поддерживаются различные температуры. Фотографии, полученные при визуализации течения методом Шлирена, показывают интересную эволюцию со временем многоячеихтых структур течения в полости при спутном противоположном направлениях тепловых и концентрационных подъемных сил. Описываются характерные детали многоячеистого течения, включающие температурные и концентрационные профили, а также приведены характеристики суммарного тепло- и массопереноса в полости.**